Emergence of unstable focused flow induced by variable-density flows in vertical fractures

Hongfan Cao[1,2], Seonkyoo Yoon[1], Zhenyu Xu[3], Laura Pyrak-Nolte[3], Etienne Bresciani[4], Peter K. Kang[1,2*]

[1]Department of Earth and Environmental Sciences, University of Minnesota, Twin Cities, Minnesota, USA.

[2]Saint Anthony Falls Laboratory, University of Minnesota, Minneapolis, Minnesota 55455, USA

[3]Department of Physics and Astronomy, Purdue University, West Lafayette, IN, United States

[4]University of O'Higgins, Rancagua, Chile

*Correspondence to: pkkang@umn.edu

ABSTRACT (<250 words)

Fluids with different densities often coexist in subsurface fractures and lead to variable-density flows that control subsurface processes such as seawater intrusion, contaminant transport, and geologic carbon sequestration. In nature, fractures have dip angles relative to gravity, and density effects are maximized in vertical fractures. However, most studies on flow and transport through fractures are often limited to horizontal fractures. Here, we study the mixing and transport of variable density fluids in vertical fractures by combining three-dimensional (3D) pore-scale numerical simulations and visual laboratory experiments. Two miscible fluids with different densities are injected through two inlets at the bottom of a fracture and exit from an outlet at the top of the fracture. Laboratory experiments show the emergence of an unstable focused flow path, which we term a "runlet." We successfully reproduce an unstable runlet using 3D numerical simulations, and elucidate the underlying mechanisms triggering the runlet. Dimensionless number analysis shows that the runlet instability arises due to the Rayleigh-Taylor instability, and flow topology analysis is applied to identify 3D vortices that are caused by the Rayleigh-Taylor instability. Even under laminar flow regimes, fluid inertia is shown to control the runlet instability by affecting the size and movement of vortices. Finally, we confirm the emergence of a runlet in rough-walled fractures. Since a runlet dramatically affects fluid distribution, residence time, and mixing, the findings in this study have direct implications for the management of groundwater resources and subsurface applications.

Keywords: vertical fracture; mixing; Rayleigh-Taylor instability; vortices; density-driven flow; focused flow

Key points

1. The density difference between injected and ambient fluids induces unstable focused flow in vertical fractures
2. Flow topology analysis is used to identify vortices that are caused by Rayleigh-Taylor instability
3. Fluid inertia controls the instability of the focused flow by affecting the size and movement of vortices, even in laminar flow regimes

Plain Language Summary

Groundwater systems are often composed of fractured rocks, and the fractures provide major pathways for groundwater flow and mass transport. Fractured rock aquifers account for about 75% of the Earth's near-surface aquifer systems, and fluids with different densities often coexist in subsurface fractures. Thus, understanding the role of variable-density fluids on fracture flows is essential for managing groundwater resources and predicting, designing, and operating many subsurface applications. The effects of density are strongest in vertical fractures; however, most previous studies on flow and transport through fractures are limited to horizontal fractures, and few have investigated the density effects on flow through vertical fractures. In this study, we report both experimental and numerical evidence of an intriguing, focused flow path caused by a density contrast between two fluids and elucidate the underlying mechanisms triggering the resulting unstable focused flow in vertical fractures, which we name a "runlet." Further, rotating flow patterns are shown to emerge and control the instability of the runlet. Since the runlet dramatically affects fluid distribution, residence time, and mixing, the findings in this study have direct implications for managing groundwater resources and subsurface applications.

1. Introduction

Fractured rock aquifers compose about 75 percent of the Earth's near-surface aquifer systems (Dietrich et al., 2005), and often contain coexisting fluids with different densities in the fractures. Understanding the role of variable-density fluids on flow, transport, and mixing in fractures is essential to predict, design, and operate many subsurface activities because fractures are the main flow paths in subsurface rocks. For example, in coastal fractured aquifers, the denser seawater can preferentially intrude through fractures saturated with freshwater (Park et al., 2012). Thus, understanding variable-density flows in fractures is important for managing water resources in coastal aquifers. Further, magma flow in dykes often involves variable density flows (Yamato et al., 2012), and variable-density fluid flows also occur during geologic CO_2 or H_2 sequestration, in which, injected less dense CO_2 or H_2 tends to migrate upwards and can leak through fractures (Tongwa et al., 2013). The leakage of CO_2 or H_2 can lead to serious consequences such as jet fire, unconfined vapor cloud explosion, and toxic chemical release (Portarapillo & di Benedetto, 2021). Variable-density flows in channels are not limited to geophysical flows; they are also very common in various industrial applications in the field of biochemical and materials engineering. Chemical samples and biological materials with different densities are often transported in channel flows in applications of these fields (Günther & Jensen, 2006; Morijiri et al., 2011). Therefore, understanding density effects on transport and mixing in channel flows is critical for the prediction, design, and operation of various applications.

Many previous studies have shown that density contrast has a significant impact on flow and solute transport in fractures (Graf & Therrien, 2005, 2007; Shikaze et al., 1998). An experimental study by Tenchine and Gouze (2005) showed that even a weak density contrast between two fluids, coupled with fracture wall roughness effects, can create preferential solute transport paths and stagnation zones that result in anomalously long tails in breakthrough curves. Even without fracture wall roughness, density contrasts have been shown to impact the flow and transport of solutes in a horizontal straight channel (Bouquain et al., 2011). Such density effects on flow and solute transport may dramatically increase when a fracture is inclined or vertical, which is common in nature. For example, Ronen et al. (1995) showed that a slight density contrast can dramatically change tracer breakthrough curves in vertical conduit flows. However,

few studies have investigated density effects on the flow and transport of variable density fluids in vertical fractures.

Further, variable-density fluid flow affects fluid mixing, which can in turn affect dissolution and precipitation patterns (Chaudhuri et al., 2009; Simmons, 2005; Tsang & Neretnieks, 1998). For example, in CO_2-brine injection experiments conducted by Ott & Oedai (2015), the mixing of CO_2 and brine formed carbonic acid that dissolved carbonate minerals. The study found that the dissolution occurred preferentially in the lower part of the horizontally oriented rock sample. Snippe et al. (2017) explained that in Ott and Oedai's experiments, gravity effects played an important role in determining the zone of preferential mixing and dissolution. Other studies, such as Oltéan et al. (2013), investigated buoyancy-driven dissolution in a vertical fracture and reported the geometrical changes of dissolution patterns over a wide range of Péclet, Damköhler, and Richardson numbers. A follow up study (Ahoulou et al., 2020) elucidated that the dissolution patterns were controlled by the level of density contrast. The density effects on mixing, dissolution, and precipitation would be much stronger in vertical fractures. However, most previous studies focused on variable-density fluid flow in porous media or horizontal fractures, and density effects on mixing and transport in vertical fractures have been elusive.

In particular, density effects may induce flow instability, which affects fluid flow, transport, and mixing. For example, the experiment on dissolution in inclined rectangular blocks showed that the dissolution patterns were affected by flow instability due to density stratification (Cohen et al., 2020). This example highlights that flow instability caused by density contrast can be critical in fracture flows. Different mechanisms have been proposed to explain the origin of instability in variable-density flows (Almarcha et al., 2010; Fernandez et al., 2002; Kneafsey & Pruess, 2010; Trevelyan et al., 2011; Wooding et al., 1997; Zalts et al., 2008). The most common explanation is Rayleigh-Taylor instability (RTI). In RTI, the displacement at the interface between two miscible fluids of different densities can lead to unstable density stratifications and fingering patterns due to gravity and buoyancy effects generated by concentration gradients. Another well-known situation that can lead to flow instability is Kelvin-Helmholtz instability (KHI). KHI occurs when there is a sufficient velocity difference across the interface between two fluids.

However, the leading mechanisms triggering flow instability in vertical fractures with variable-density fluids remain unclear.

In this study, we report both experimental and numerical evidence of an intriguing, focused flow path caused by a density contrast between two fluids and investigate the underlying mechanisms triggering the resulting unstable focused flow in vertical fractures. 3D numerical simulations are conducted for a wide range of controlling factors, including density contrast, flow rate, solute diffusivity, and fracture roughness. Flow topology analysis is conducted to analyze the complex 3D flow fields and to identify the locations and number of vortices that control the instability of focused flow. Further, dimensionless number analysis is used to elucidate the underlying mechanisms triggering the observed instability, and we extend the findings to a rough fracture.

The remainder of this article is organized as follows. The experiment and simulation setups are detailed in Section 2. The results are given and discussed in Section 3. In Section 4, we summarize our key findings and conclusions.

2. Methods

2.1 Experimental and numerical simulation setup

Fracture flow is often simplified as the flow between two parallel flat plates, known as Hele-Shaw flow (Al-Bahlani & Babadagli, 2012; Chen, 1989; Saffman & Taylor, 1958). In this study, we start with a vertical flow cell with parallel flat plates and then extend the findings to rough fractures. A Hele-Shaw cell is an idealized but good proxy for identifying critical flow and fluid related factors that affect variable-density flow and solute transport in a vertical fracture. For visual laboratory experiments, we used two flat transparent polycarbonate sheets (100 mm by 100 mm by 12.7 mm) separated by spacers to form a fracture with a uniform aperture of 4 mm. Two nonreactive miscible fluids with different densities (Fluid 1 and Fluid 2) were introduced through two inlets at the bottom of the fracture and exited through a single, elongated outlet at the top of the fracture (Figure 1(a, b)). The size of the two inlet ports was 3 mm × 3 mm, and the rectangular outlet port was 3 mm × 60 mm. The two inlets were placed 38 mm apart at the bottom of the system. The fluid and flow related conditions used in the laboratory experiment

(case 1) are listed in Table 1. The denser fluid (Fluid 1) contained a dye (Brocresol green) to enable the imaging of fluid distributions. Readers are referred to Xu (2020) for additional experimental details.

Numerical simulations were used to investigate the effects of density contrasts, injection rates, diffusion, and fracture roughness on variable-density flows in a vertical fracture. Figure 1 (c) shows the simulation setup that is based on the laboratory experimental setup, and Figure 1 (d) provides a simulated image of the concentration distribution, in which the concentration value is proportional to Fluid 1 concentration. The entire domain was discretized into 400×400×16 cells. All boundaries were set to no-slip boundaries except for the inlets and outlet. We simulated a total of ten cases to study the effects of density contrasts, injection rates, diffusion, and roughness. Table 1 lists the fluid and flow-related parameters for all the numerical cases. The reference case (case 1) refers to the case in which the conditions were identical to those in the laboratory experiment. The parameters that differ from the reference case are shown in boldface.

Table 1. Fluid and flow related parameters used in the numerical study cases

		Density ($\frac{kg}{m^3}$)	Dynamic viscosity ($Pa \cdot s$)	Injection rate ($\frac{ml}{min}$)	Diffusion coefficient ($\frac{m^2}{s}$)
Case 1 (Reference case)	Fluid 1	1111	1.20×10^{-3}	0.17	10^{-9}
	Fluid 2	1031.8	1.11×10^{-3}	1.36	
Case 2	Fluid 1	**1031.8**	1.20×10^{-3}	0.17	10^{-9}
	Fluid 2	1031.8	1.11×10^{-3}	1.36	
Case 3	Fluid 1	1111	1.20×10^{-3}	0.17	$\mathbf{10^{-6}}$
	Fluid 2	1031.8	1.11×10^{-3}	1.36	
Case 4	Fluid 1	1111	1.20×10^{-3}	0.17	$\mathbf{10^{-7}}$
	Fluid 2	1031.8	1.11×10^{-3}	1.36	

Case 5	Fluid 1	1111	1.20×10^{-3}	0.17	$\mathbf{10^{-8}}$
	Fluid 2	1031.8	1.11×10^{-3}	1.36	
Case 6 **(non-inertial)**	Fluid 1	1111	1.20×10^{-3}	0.17	10^{-9}
	Fluid 2	1031.8	1.11×10^{-3}	1.36	
Case 7	Fluid 1	1111	1.20×10^{-3}	0.17	10^{-9}
	Fluid 2	1031.8	1.11×10^{-3}	**0.17**	
Case 8 **(rough fracture)**	Fluid 1	**1031.8**	1.11×10^{-3}	0.17	10^{-9}
	Fluid 2	1031.8	1.11×10^{-3}	1.36	
Case 9 & 10 **(rough fracture)**	Fluid 1	1111	1.20×10^{-3}	0.17	10^{-9}
	Fluid 2	1031.8	1.11×10^{-3}	1.36	

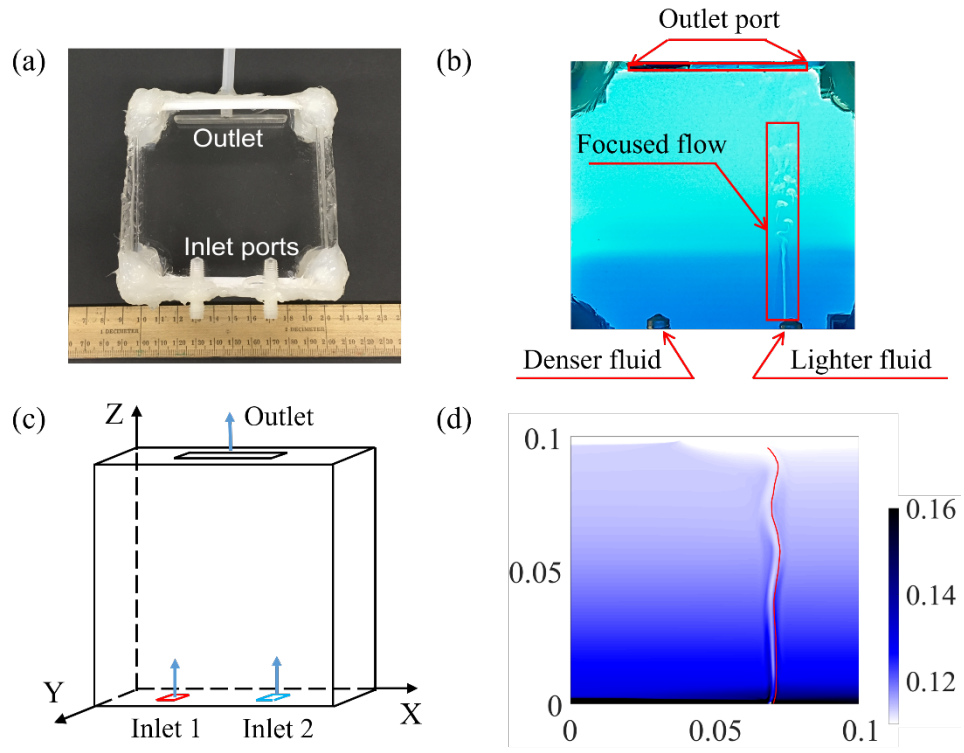

Figure 1. (a) Experimental setup used in the laboratory experiment. (b) A snapshot from a laboratory experiment. The fracture aperture is 4 mm, injection rate is 0.17 ml/min for lighter

fluid, 1.36 ml/min for denser fluid, and density ratio is 1111/1031.8. (c) Setup and boundary conditions of the numerical model. (d) A snapshot of depth averaged concentration distribution obtained from the numerical simulation. Concentration values represent the relative concentration of Fluid 1. The injection rates and the fluid densities are identical to the laboratory experiment.

2.2 Governing equations and numerical solution

Three-dimensional pore-scale numerical simulations are conducted to study the variable-density flow and transport of miscible fluids of different densities in a vertical fracture. We used OpenFOAM (Weller et al., 1998), an open-source CFD software developed by OpenCFD Ltd to perform the simulations. Fluid flow in a fracture can be described by the Navier-Stokes (N-S) equations that consider the mass and momentum conservations:

$$\frac{\partial \rho}{\partial t} + \nabla \cdot (\rho u) = 0 \tag{1}$$

$$\frac{\partial (\rho u)}{\partial t} + \nabla \cdot (\rho u u) = -\nabla p + \rho g + \nu \nabla^2 u \tag{2}$$

where u is the velocity field, p is the pressure field, ρ is the fluid density, g is the gravitational acceleration, and ν is the kinematic viscosity. Solute transport in a fracture is described by the advection-diffusion equation (ADE):

$$\frac{\partial C}{\partial t} + \nabla \cdot (uC) - D\nabla^2(C) = 0 \tag{3}$$

where C is the passive solute concentration that is injected with Fluid 1 (denser fluid), and D is the diffusion coefficient. Thus, the concentration is one when the fluid is composed purely of Fluid 1 (denser fluid) and the concentration is zero when the fluid is composed purely of Fluid 2 (lighter fluid).

Since the density variability in our system arises due to the two miscible fluids with different densities, the fluid density ρ can be expressed as a linear function of concentration C:

$$\rho = \rho_0 + \frac{\partial \rho}{\partial C}(C - C_0) \tag{4}$$

where C_0 is the reference concentration of the lighter fluid which we set to be zero, and ρ_0 is the reference density at the reference concentration. Thus, equation (2) and equation (3) are coupled

198 through equation (4) in a nonlinear way: the change of concentration distribution affects the fluid
199 density, which in turn affects the flow field. In our system, we can make the Boussinesq
200 approximation (Gartling & Hickox, 1985; Gray & Giorgini, 1976) that simplifies the flow
201 equations. The Boussinesq approximation is valid when the density variability is small and when
202 the gravity force term in the momentum equation is significantly larger than the inertia term,
203 which is the case of this study (Hamimid et al., 2021; Huang et al., 2020). The maximum
204 Reynolds number ($Re = \frac{ul}{\nu}$) considered in this study is around 10, which is obtained using the
205 fracture aperture as l and the maximum injection velocity as u. This indicates that the flow is in
206 the laminar regime (Wood et al., 2020). With the Boussinesq approximation, the equations (1)
207 and (2) can be simplified to

208 $$\nabla \cdot u = 0 \tag{5}$$

209 $$\rho_0 \left(\frac{\partial u}{\partial t} + u \cdot \nabla u\right) = -\nabla p + \rho g + \nu \nabla^2 u \tag{6}$$

210 We solve equations (5), (6) for fluid flow, equation (3) for transport, and flow and transport
211 equations are coupled through equation (4).

212

213 2.3 Flow topology analysis

214 Various flow topologies can emerge in 3D velocity fields (Bakker & Berger, 1991; Perry &
215 Chong, 1994; Délery, 2013; Romanò et al., 2017). In particular, the flow fields of variable-
216 density flows can be complex and thus challenging to characterize (Stein et al., 1989; Contreras
217 et al., 2017; Hidalgo & Dentz, 2018; Bresciani et al., 2019; Lee & Kang, 2020). A powerful way
218 to analyze complex 3D velocity fields is by identifying and tracking the essential structures of a
219 flow field using the concept of vector field topology (Asimov, 1993; Globus et al., 1991; Helman
220 & Hesselink, 1989; Perry & Fairlie, 1975; Theisel et al., 2008). Vector field topology reduces
221 flow complexity through the identification of the topological features of the flow field (e.g.,
222 stagnation points, dividing stream surfaces), which constitutes the backbone of a flow field.
223 Moreover, tracking these topological features over time or over a change in system parameters
224 provides insight into the dynamics of the system (Theisel et al., 2005; Lester et al., 2009; Cirpka
225 et al., 2015; de Barros et al., 2012).

226

Stagnation points constitute key information about a flow field and thus the identification of stagnation points is an important step in the topology analysis. For a 3D vector field $v(x)$, a stagnation point x_0 is extracted by finding $v(x_0) = 0$ with $v(x_0 \pm \varepsilon) \neq 0$ (where ε is an arbitrarily small quantity) and is classified based on the eigenvalues λ_i $(i = 1..3)$ of the Jacobian matrix of the 3D vector field $J(x_0)$. Depending on the sign of the real parts of the eigenvalues $Re(\lambda_i)$, the stagnation points can be classified into four non-degenerate types: sources, sinks, repelling saddles, and attracting saddles:

$$Sources: \quad 0 < Re(\lambda_1) \leq Re(\lambda_2) \leq Re(\lambda_3)$$

$$Repelling\ saddles: \quad Re(\lambda_1) < 0 < Re(\lambda_2) \leq Re(\lambda_3)$$

$$Attracting\ saddles: \quad Re(\lambda_1) \leq Re(\lambda_2) < 0 < Re(\lambda_3)$$

$$Sinks: \quad Re(\lambda_1) \leq Re(\lambda_2) \leq Re(\lambda_3) < 0$$

Degenerate types only arise rarely (Perko, 2001), and so they are disregarded. The flow patterns around the four types of stagnation points are fundamentally different. Sources and sinks consist of outflow and inflow, respectively. A repelling saddle has one direction of inflow and two directions of outflow, while an attracting saddle has one direction of outflow and two directions of inflow. Each of these types can be further divided into two types according to the imaginary parts of the eigenvalues $Im(\lambda_i)$:

$$Focus: \quad Im(\lambda_1) = 0\ and\ \ Im(\lambda_2) = -Im(\lambda_3) \neq 0$$

$$Nodes: \quad Im(\lambda_1) = Im(\lambda_2) = Im(\lambda_3) = 0$$

Note that here and above, the numbering of the eigenvalues does not matter. For the focus type, there is a rotating pattern in the inflow or outflow plane, whereas for the node type, the flow lines are asymptotically straight when approaching the stagnation point. These eight types of 3D stagnation points are visualized in Figure 2. In this study, we identify focus saddle type stagnation points, which are associated with vortices (Figure 2(f, h)). We relied on a VTK-based open-source code to identify the stagnation points and their type (Bujack et al., 2021).

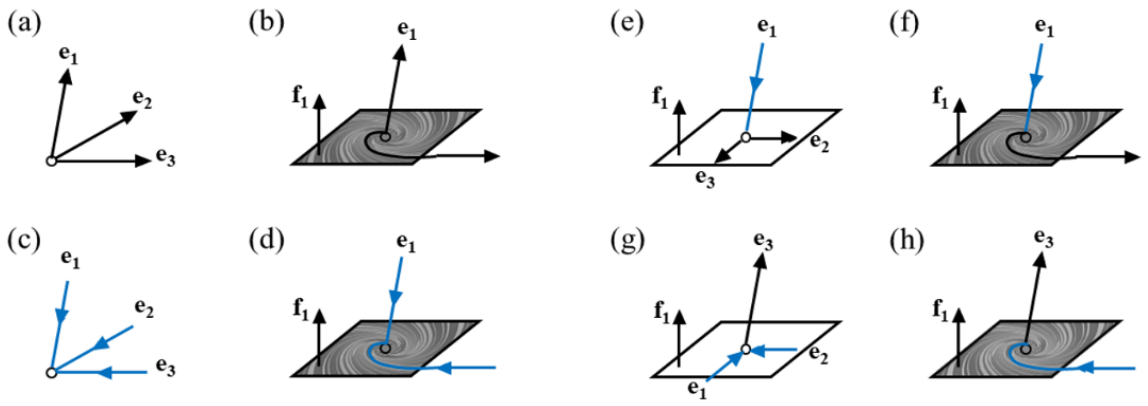

Figure 2. Eight common types of stagnation points in 3D vector fields (modified from Weinkauf & Tino, 2008). Repelling focus saddle (f) and attracting focus saddle (h) type stagnation points are associated with vortices, and thus we identify those stagnation points in this study.

3. Results and discussion

3.1 The origin of the runlet

In the laboratory experiments, the fracture sample was initially filled with the lighter fluid. Then, simultaneously, the denser fluid was continuously injected from the left inlet and the lighter fluid was continuously injected from the right inlet. Experimental results show that the lighter fluid was confined to a narrow path in a vertical fracture. The narrow path is not straight and the shape of the narrow path continuously changes in time (Figure 1(b)). In this paper, we term the narrow path of the lighter fluid as a "runlet" and denote the continuous change (fluctuation) of runlet shape as the "runlet instability". The numerical result of the reference case is shown in Figure 1(d). The concentration values were averaged in the aperture direction to obtain the depth averaged concentration field. The simulation successfully reproduces the key features of the experimental results such as the formation of the runlet and the instability of the runlet (Figure 1(d)). However, small-scale features such as the mushroom-shaped lighter fluid parcels observed

in the experiment (runlet in lighter blue region in Figure 1(b)) is not evident in the simulation results. This can be attributed to the grid resolution and numerical dispersion.

In both the laboratory experiments and numerical simulations, the lighter fluid was confined by the denser fluid. We hypothesize that the density contrast between the two fluids causes the runlet. To test this hypothesis, we simulated case 2, where the experimental conditions are identical to the reference case but without the density contrast (Table 1). In other words, two fluids with different densities are injected in the reference case, while two fluids with the same density are injected in case 2, i.e., $\frac{\partial \rho}{\partial c} = 0$. Figure 3 shows the concentration distributions and streamlines from the two simulation cases. From the concentration distribution of the reference case (Figure 3(a)), we can clearly observe that the lighter fluid is confined to an unstable runlet. Whereas in case 2, there is no runlet (Figure 3(c)), and the streamlines are smooth and relatively straight (Figure 3(d)). The larger injection rate of Fluid 2 causes Fluid 2 to occupy more space compared to Fluid 1, and there is limited mixing between the two fluids, as shown by the segregation of the fluids. This demonstrates that the density difference between the two injected fluids underpins the formation of the unstable runlet in the vertical fracture and also strongly affects the overall fluid mixing.

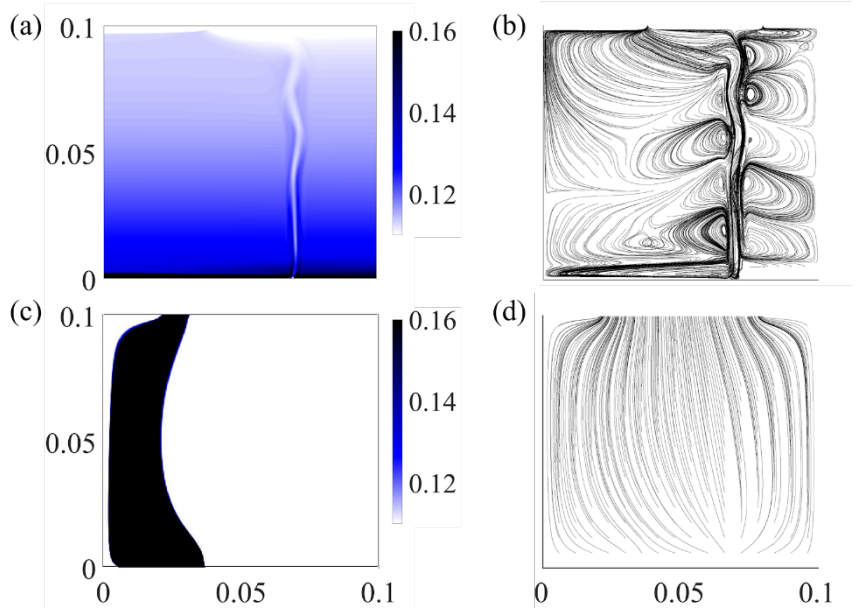

Figure 3. (a) Depth averaged concentration distribution of case 1 (the two fluids have different densities). The lighter fluid is confined to a runlet. (b) Streamlines of case 1. The streamlines

clearly visualize the runlet and the emergence of vortices along the runlet. (c) Depth averaged concentration distribution of case 2 (the two fluids have the same density). (d) Streamlines of case 2. Note that in both cases the injection rate of Fluid 2 (right inlet) is larger than the injection rate of Fluid 1 (left inlet).

From the concentration distribution shown in Figure 3(a), we find that the interface between the lighter and denser fluids is not sharp. The diffused interface of two fluids in the reference case (case 1) is caused by the active mixing between the two fluids along the runlet. Mixing will reduce the density difference between the runlet and background fluid, and the runlet may disappear for enhanced mixing conditions. The mixing between two fluids is controlled by fluid stretching and diffusion (Dentz et al., 2011; le Borgne et al., 2013, Yoon et al., 2021). Fluid stretching due to velocity heterogeneity is known to control mixing by controlling the length elongation and width compression of mixing zone near the fluid interface. Vortices that appear near the runlet seem to enhance fluid stretching, and diffusion ultimately mixes the two fluids. If the diffusion coefficient is larger, the mixing of the two fluids will be enhanced and the density gradient between the runlet and background fluid will decrease, which may lead to the eventual disappearance of the runlet.

To study the effects of mixing on the density contrast and the runlet formation, we considered three cases with different diffusion coefficients (cases 3 to 5 in Table 1) and compared the results with the reference case. If the density contrast is the origin of runlet formation, it is expected that the runlet will not form or will dissipate for high enough diffusion coefficients. The diffusion coefficient is 10^{-9} m^2/s in the reference case and was varied from 10^{-6} to 10^{-8} m^2/s in cases 3 to 5. The concentration distributions and streamlines of cases 3-5 are shown in Figure 4. For case 3 with the highest diffusion coefficient of 10^{-6}, the two fluids mix well, leading to the disappearance of the runlet. For case 4, in which the diffusion coefficient is 10^{-7}, the runlet is visible near the inlet but it is relatively short and stable (Figure 4(c)). From the streamlines in Figure 4(d), we observe that the vortical flows are only present near the inlet and then the streamlines disperse rapidly. For case 5 (Figure 4(e-f)), in which the diffusion coefficient is smaller, we clearly observe an unstable runlet, but there are fewer vortical flow structures than in the reference case (Figure 4(g-h)) which has the smallest diffusion coefficient. These results

confirm that the formation of the runlet and the presence of vortical flows along it are strongly affected by the mixing of the two fluids. Only when the diffusion coefficient is small enough, the density contrast between the lighter fluid and the background fluid is large enough to sustain the narrow runlet and to induce vortical flows.

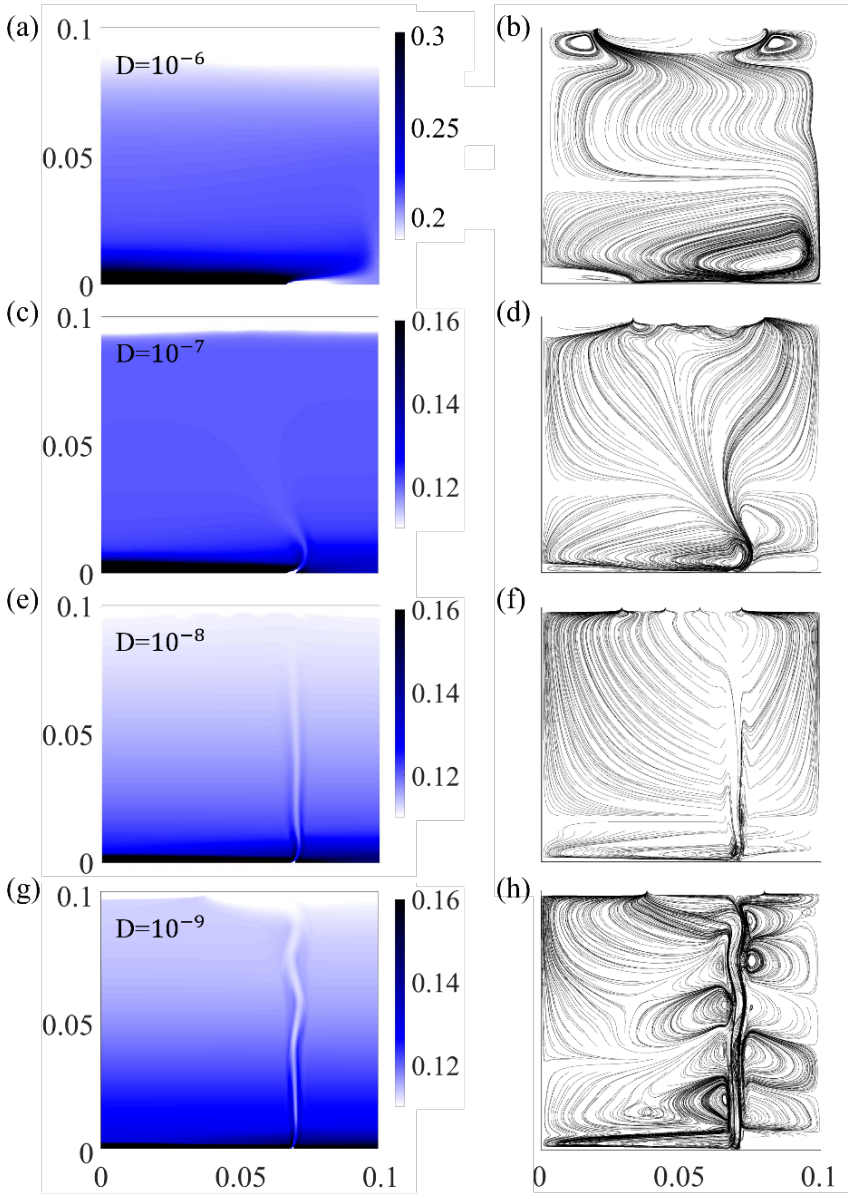

Figure 4. (a) Depth averaged concentration distribution of case 3 ($D=10^{-6}$ m^2/s). (b) Streamlines of case 3. (c) Depth averaged concentration distribution of case 4 ($D=10^{-7}$ m^2/s). (d) Streamlines of case 4. (e) Depth averaged concentration distribution of case 5 ($D=10^{-8}$ m^2/s). (f) Streamlines of case 5. (g) Depth averaged concentration distribution of case 1 ($D=10^{-9}$ m^2/s; reference case). (h) Streamlines of case 1.

3.2 Runlet instability and flow topology analysis

As defined in section 3.1, the runlet instability means the fluctuation and the continuous change of runlet shape in time. To quantify the level of fluctuation of the runlet, we identified the centerline along the runlet by identifying the location of the minimum concentration on each horizontal x-y plane and tracing those points in the vertical direction (the redlines in Figure 1(d) and Figure 5(b)). Note that we discretized the domain into 400 horizontal layers with a thickness of 0.25 mm. We define the traced line of minimum concentration as the centerline of the runlet, and the length of the centerline represents the length of the runlet. We can then track the length of the runlet in time. Figure 5(a) shows the change in the length of the centerline (runlet) in time. We observe that the length of the centerline increases roughly linearly in time and then asymptotes to a constant value. This indicates that the runlet becomes longer and unstable over time and eventually reaches a quasi-steady state where the instability does not intensify further nor dissipate. At the quasi-steady state, the runlet continues to fluctuate as shown in the supplementary video.

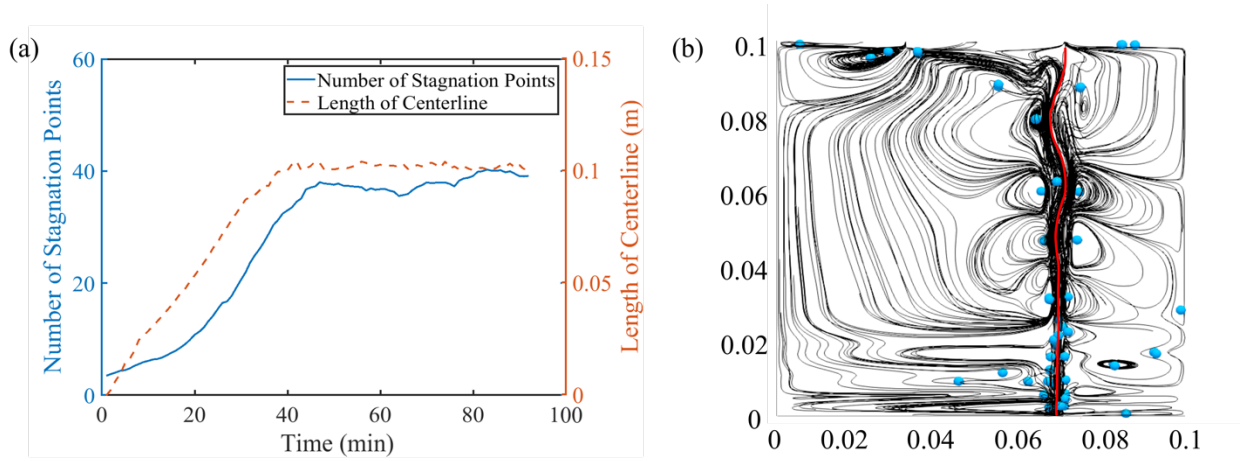

Figure 5. (a) Number of focus saddles (repelling or attracting) and length of the centerline as a function of time. (b) Location of focus saddles at a snapshot of the reference case. Blue circles show the location of identified focus saddles, and the redline shows the centerline.

From the streamlines of the reference case (Figure 3(b)), we observe that a number of vortices occur along the runlet. Critical stagnation points associated with the vortices were extracted

using a topology analysis tool (Bujack et al., 2021). We analyzed the focus saddles (Figure 2(f)(h)) because the spiral flow around these stagnation points has the same flow pattern as vortices. The identified focus saddles are shown with blue circles in Figure 5(b). Most of them are indeed located at the center of vortices or near the vortices. Thus, the number of focus saddles are an indicator of the number of vortices. The stagnation points are densely populated near the inlet, and the number decreases in the vertical (flow) direction. In other words, more vortices exist near the lower part of the system, which is also where the concentration gradients are higher. High concentration gradients at the lower part of the system may lead to RTI (Kull, 1991; Sharp, 1984), and the vortices produced by RTI may be the origin of the runlet instability. The relation between RTI, vortices, and runlet instability will be further discussed in the following section.

The spiral flows around vortices affect the flow pattern around the runlet, bending the runlet and leading to the instability of the runlet. To check if the vortices are playing a crucial role in causing the runlet instability, we calculated the total number of focus saddles and plot the total number of these stagnation points over time. The trends of the number of stagnation points and that of the length of the centerline are almost identical (Figure 5(a)). This result suggests that the number of stagnation points, especially the number of focus saddles, can be used to quantify the instability of the runlet, and the instability of the runlet is strongly affected by the vortices.

3.3 Origin of runlet instability: Rayleigh-Taylor instability versus Kelvin-Helmholtz instability

Here, we investigate the origin of the vortices that control the instability of the runlet over time. Vortical flows can be generated by either concentration gradients or velocity gradients in our system. The concentration and velocity distribution at multiple horizontal cross sections (at z = 25 mm, 50mm, and 75 mm from the bottom of the domain) at three pore volume injection (PVI) are shown in Figure 6. One PVI is equivalent to the time required for the injected fluid volume to reach the total pore volume of the fracture domain (pore volume divided by injection rate). From the concentration maps (Figures 6(a),(c),(e)), a large concentration gradient around the runlet is evident. In particular, the concentration at the perimeter of the runlet is higher than that in other areas, showing the non-monotonic concentration profile. Note that during injection, the denser fluid sinks to the bottom of the fracture due to gravitational effects, displacing the lighter fluid

that initially filled the fracture. As both fluids are continuously pumped into the fracture, the denser fluid occupies most of the fracture near the inlet, except where the runlet is. The runlet is formed by the injected lighter fluid, thus having a low concentration. The runlet has a high velocity because the lighter fluid is flowing through a narrow runlet. Thus, the denser fluid near the runlet moves along with the lighter fluid due to shear drag exerted by the high-velocity runlet flow. This explains the maximum fluid concentration at the perimeter of the runlet.

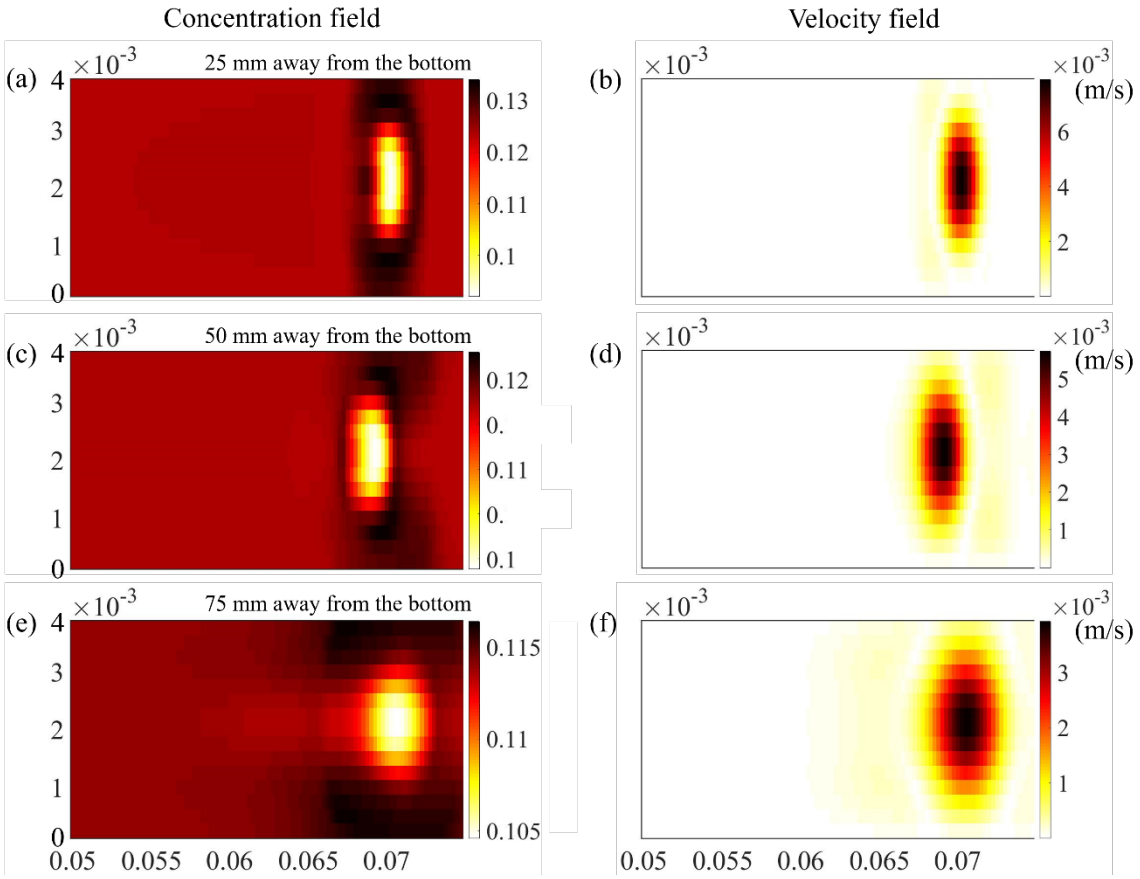

Figure 6. Concentration and velocity fields in cross sections at (a) (b) 25 mm, (c) (d) 50 mm, and (e) (f) 75 mm from the bottom of the domain. Concentration around the runlet is higher than in other areas. Velocity is greatest at the runlet center.

The instability of the interface between two fluids caused by different densities is known as Rayleigh-Taylor instability (RTI) (Kull, 1991; Sharp, 1984; He et al., 1999; Tryggvason, 1988). Here, we qualitatively describe the overall process induced by RTI and quantitatively confirm the discussed processes in the following sections. The density contrast between the runlet and

surrounding fluid can lead to opposing flow directions between the denser and lighter fluids. At an early stage, the denser fluid at the bottom of the fracture and near the runlet is pulled along the runlet because of the injection force (Figure 7 I). This is due to the drag force exerted on the surrounding denser fluid by the fast-flowing lighter fluid. Then, due to the density effect, the denser fluid sinks to the bottom of the fracture and mixes with the surrounding fluid causing RTI. This is how a rotating flow pattern (vortex) emerges at the bottom of the fracture (Figure 7 II). Subsequently, the vortex moves upward due to the drag force along the runlet, and the runlet bends due to the spiral flows (Figure 7 III). The upward movement of vortices are shown in the supplementary video. As the vortex rises, the same phenomenon occurs on the other side of the runlet and another vortical flow emerges. Thus, vortices emerge on either side of the runlet, leading to a the runlet bending in alternating directions (Figure 7 IV). Figure 7 is a schematic showing the step-by-step process.

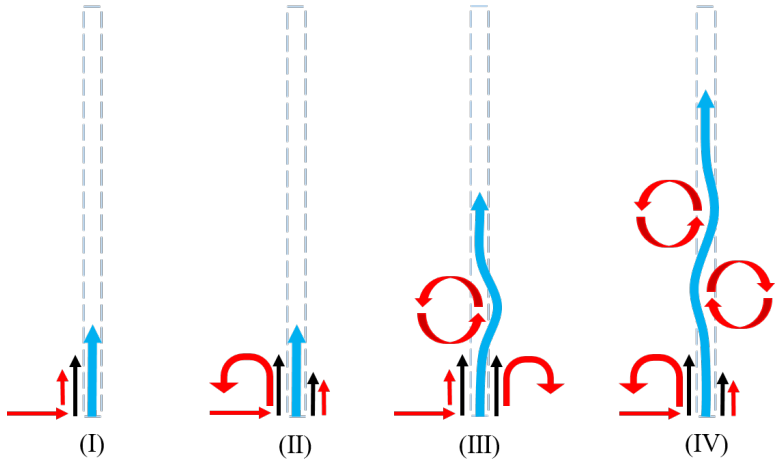

Figure 7. Developmental stages of vortices and unstable runlet. Blue arrows show the movement of the lighter fluid, black arrows show drag force exerted on the denser fluid by the runlet, and red arrows show the movement of the denser fluid.

The Rayleigh (Ra) number is a dimensionless number that is commonly used to predict and describe the instability of variable-density flows. Ra is the ratio comparing the convective mass transfer and the diffusive mass transfer. When Ra is greater than some critical Rayleigh number, Ra_c, the density-driven convective transport is dominant, and the spiral vortical flows result from the RTI (Cengel et al., 2001; le Quere, 1990; Solano et al., 2022). The critical Rayleigh number allows us to predict the occurrence of RTI, and the value is dependent on a given experimental

setup. We quantify Ra using the following definition that is based on the concentration gradient (Hage & Tilgner, 2010; Ślezak et al., 2004):

$$Ra = \frac{g\alpha l^4}{D\nu}\frac{\partial C}{\partial s} \quad (7)$$

where $\frac{\partial C}{\partial s}$ is the concentration gradient and $\alpha = -\frac{1}{\rho}\frac{\partial \rho}{\partial C}$ describes the density change with regard to concentration. We estimated Ra along the z-direction for different diffusion coefficients (reference case and cases 3 to 5 in Table 1). The representative length l of the fluid volume is taken to be half of the fracture aperture (2 mm). The entire domain is divided into 400 horizontal layers, and Ra is calculated for each layer. In each horizontal layer, the locations of the maximum and minimum concentration values are identified. Then, ∂C is obtained by taking the concentration difference between these two points, and ∂s is obtained by estimating the distance between the two points. Figure 8 shows the estimated Ra in the z-direction.

As shown in Figure 8, Ra decreases as the diffusion coefficient increases because stronger diffusion leads to a reduced concentration difference. For the case in which the diffusion coefficient is 10^{-7} (red line), the maximum Ra is ~ 7×10^5, and when the diffusion coefficient is 10^{-8} (green line), the maximum Ra is ~ 1.3×10^6. Considering that the runlet is relatively stable in the case with a diffusion coefficient of 10^{-7} (red line), and the runlet becomes unstable in the case for a diffusion coefficient of 10^{-8} (green line), we can infer that the instability emerges when Ra is somewhere between 7×10^5 and 1.3×10^6 (the gray zone in Figure 8). Therefore, the critical Rayleigh number (at which the runlet becomes unstable) is in the order of 1×10^6. For the cases with the diffusion coefficient of 10^{-8} and 10^{-9} (green and blue lines, respectively), Ra is larger than Ra_c only near the inlet. This implies that the vortices, which control the instability, can only originate near the lower part of the system. Indeed, it can be observed from Figure 5(a) that most of the vortices are indeed located near the injection port. Although the Ra at the upper part of the system is smaller than Ra_c, the vortices can travel upwards with the flow because of the injection force and lead to the bending and instability of the runlet. The supplementary video confirms that the instability in the upper part is governed by the vortices migrated from the bottom part.

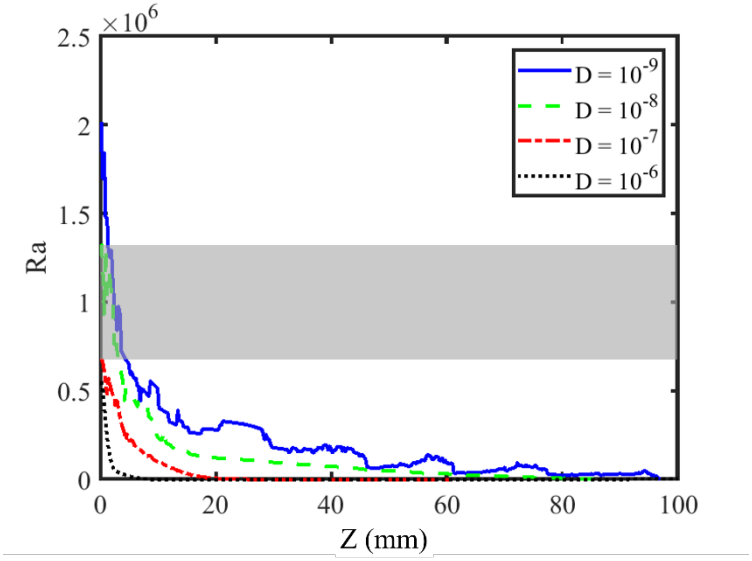

Figure 8. Evolution of Rayleigh number (Ra) as a function of vertical location (z) for different diffusion coefficients. z = 0 mm at the bottom of the fracture (where the inlet is located).

Another well-known mechanism that can lead to flow instability is the Kelvin-Helmholtz instability (KHI) (Funada & Joseph, 2001; Smyth & Moum, 2012). KHI occurs when there is a sufficient velocity difference across the interface between two fluids. The large velocity shear can induce instability along the interface. Therefore, the interface becomes an unstable vortex sheet. From the velocity fields at different cross sections (Figure 6(b),(d),(f)), we observe a rapid change in the velocity magnitude near the runlet, which may lead to KHI. For KHI, the Richardson number (Ri) is the dimensionless number that is used to predict the instability. Ri represents the ratio of the buoyancy term to the flow shear term:

$$Ri = \frac{g}{\rho} \frac{\frac{\partial \rho}{\partial s}}{\left(\frac{\partial u}{\partial s}\right)^2} \tag{8}$$

where $\frac{\partial u}{\partial s}$ is the velocity gradient. When the Richardson number is below the critical Richardson number Ri_c, the fluid becomes unstable. In other words, the fluid flow should be stable if Ri of the system has Ri that is significantly larger than Ri_c. Therefore, we estimate the minimum Ri that our system can reach. If the minimum Ri is much larger than Ri_c, we can conclude that the KHI is not the cause of the instability. To obtain the smallest Ri that can occur in our system, we estimate the largest velocity difference ∂u. The maximum velocity difference possible in our system is the

injection velocity. Thus, the maximum ∂u is taken as the injection velocity, which is around 2.5 $\mathrm{mm/s}$. ρ is taken as the density of the lighter fluid, which is 1031.8 kg/m^3. ∂s is taken as half of the fracture aperture, which is 2 mm, and $\partial \rho$ is taken as the density difference between the lighter and denser fluid, which is 79.2 kg/m^3. Using these numbers, the smallest Ri in the system is estimated to be about 240. The values of $\mathrm{Ri_c}$ from previous studies range from 0.2 to 1.0 (Abarbanel et al., 1984; Galperin et al., 2007; Howard, 1961). Considering the Ri calculated in our system is two orders-of-magnitude larger than the $\mathrm{Ri_c}$, the RTI appears to be the main mechanism that makes the runlet unstable.

3.4 Influence of inertial force

From Figure 5(b), we observe that more stagnation points are present near the inlet and the number decreases in the flow (vertical) direction. This is because more vortices appear at the lower part of the system due to the high concentration gradient near the inlet. As we discussed before, the spiral flow around vortices makes the runlet unstable. Intuitively, more vortices should lead to more unstable runlet. However, in both experiment and simulation results (Figure 1(b)(d)), we observed that runlets are stable and straight near the injection point (lower part) and become unstable as the distance from the inlet increases. One reason for the stability may be due to the high inertial force of lighter fluid near the inlet, suppressing the effects of vortical flows. To investigate the influence of inertial force on the stability of the runlet, we considered case 6 that solves Stokes equations instead of Navier-Stokes equations to simulate non-inertial flow. Stokes equations can be obtained by removing the inertial terms in the momentum balance equation (2):

$$\frac{\partial(\rho u)}{\partial t} = -\nabla p + \rho g + \nu \nabla^2 u \tag{9}$$

After applying the Boussinesq approximation, Equation (9) can be written as:

$$\rho_0 \frac{\partial u}{\partial t} = -\nabla p + \rho g + \nu \nabla^2 u \tag{10}$$

The parameters of the fluid used in this case are the same as the reference case in Table 1. We compare this case (case 6) with the reference case (case 1) where we account for the inertial force. The concentration distributions and streamlines of the case that neglect inertial force are

shown in Figure 9 (a)(b). Results show that in both cases, the upper half part of the runlet is unstable, and the wavelengths are similar. However, in the case that the inertial force is neglected, the instability initiates near the inlet and the upward movement of vortices are limited, which is clearly different from the case considering the inertia (supplementary video). The results are consistent with the hypothesis that in the case considering the inertial force, although vortices emerge at the lower part of the system as predicted by the high Rayleigh number, the large inertial force caused by the fast runlet flow maintains the straightness of the runlet near the inlet. As we discussed in section 3.3, the vortices travel up along with the flow because of the injection force. In the upper part, due to the decrease in inertial force, the vortical flow effect dominates over injection force, so the runlet shows enhanced fluctuations. In the case that neglects the inertial force, the vortices appearing at the lower part can lead to the fluctuation of the entire runlet, but the vortices show limited upward movement due to the lack of inertia force.

To further study the effects of inertial force on the runlet stability, we simulated case 7 with a smaller injection rate of the lighter fluid than the reference case (case 1). The inertial force increases as the injection rate increases. In case 7 shown in Table 1, the injection rate of the lighter fluid is the same as the injection rate of the denser fluid, which is 0.17 ml/min, an order of magnitude smaller than the lighter fluid injection rate in the reference case. From the concentration distributions (Figure 9(f)) of case 7, although the inertial force is smaller, the lower part of the runlet is still straight due to the inertial force. Further, the upper part of the runlet is unstable in both cases but the wavelength in case 7 is significantly shorter than that in the reference case, which is consistent with what is observed in laboratory experiments (Xu et al., 2022). Studies on confined laminar impinging slot-jets also reported that the size of a vortex increases with increasing Reynolds number (Sexton et al., 2018; Sivasamy et al., 2007). From case 7, we can conclude that the increase in injection rate of lighter fluid increases the wavelength of the runlet, which is associated with the size of vortices. These findings highlight that the inertia effect can be critical for fracture flows even in the laminar flow regimes.

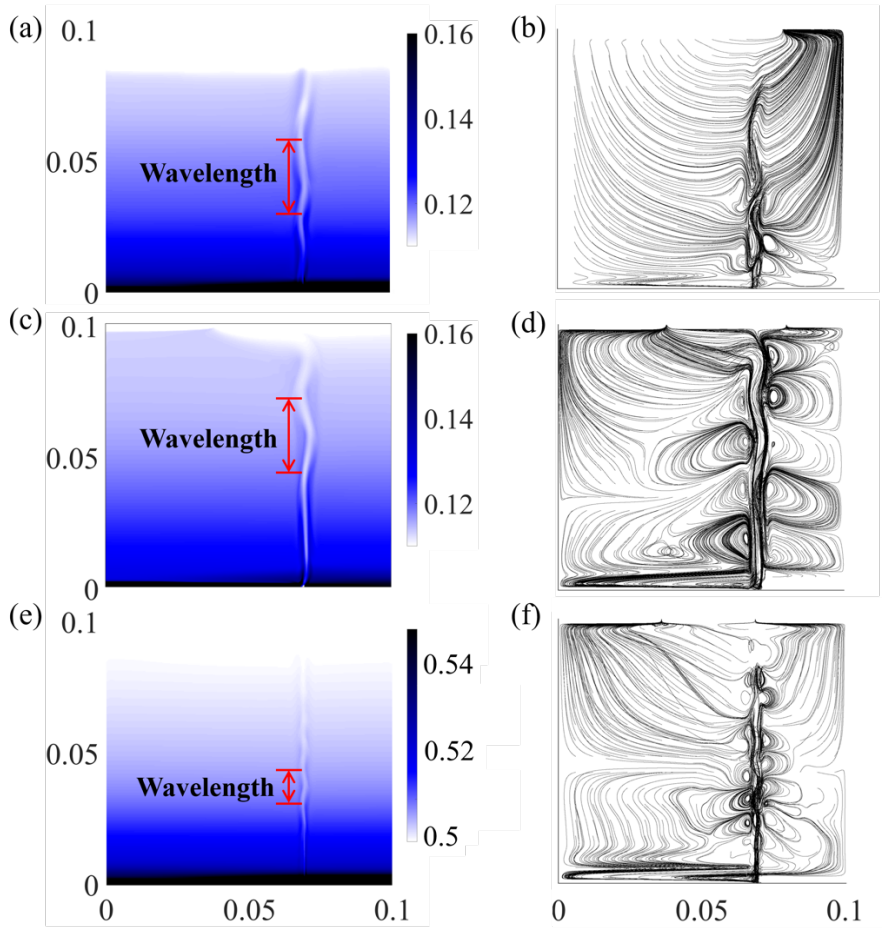

Figure 9. (a) Depth averaged concentration distribution of the case 6 that neglects inertial force. (b) Streamlines of the case 6 that neglects inertial force. (c) Depth averaged concentration distribution of the reference case. (d) Streamlines of the reference case. (e) Depth averaged concentration distribution of the case 7, in which the injection rate of lighter fluid is 0.17 ml/min. (f) Streamlines of the case 7, in which the injection rate of lighter fluid is 0.17 ml/min.

3.5 Effects of fracture roughness and aperture variability

Fracture surfaces are rough in nature, and fracture roughness is known to significantly affect fluid flow and transport. For example, aperture variability due to surface roughness can lead to preferential flow paths and stagnation zones (Kang et al., 2016; Tsang & Neretnieks, 1998; Yoon & Kang, 2021). To study the effects of surface roughness on runlet, we conducted 3D numerical simulations on a real rock fracture geometry (case 8, 9, 10). The surface topography data obtained by scanning a natural fracture (Sawayama et al., 2021) and was used to generate a

rough fracture. We chose an area of 100 mm × 100 mm from the dataset. Figure 10 (a) shows the aperture map between the two rough fracture surfaces. The mechanical aperture (the average distance between the two fractures surfaces) is fixed to be 4 mm such that it is consistent with the cases with parallel plates. Figure 10 (b) shows the cross sections of the rough fracture at four different locations. Generally, the lower half of the fracture has larger aperture than the upper half.

To investigate density effects on runlet formation in rough fractures, we first simulated the case in which the two fluids have the same density (case 8). The fluid properties we used in this case are the same as case 2 (Table 1). No runlet is formed in the rough fracture without density contrast (Figure 10 (c-d)), which confirms that the density contrast between two fluids injected is critical to the formation of the runlet also in a rough fracture. We then considered the case in which the two fluids have the density difference (case 9). The injection position of the lighter fluid is indicated by the blue arrow in Figure 10 (a). The concentration distribution (Figure 10 (e)) clearly shows that the runlet of lighter fluid is present and unstable in the rough fracture case. The streamlines (Figure 10 (f)) show that there are vortices along the runlet, and they make the runlet to be unstable, similar to that observed in the uniform aperture fracture (i.e., parallel plates).

To further study the effects of fracture roughness on the formation and instability of the runlet, we simulated an additional case (case 10) by rotating the fracture. The injection location of lighter fluid for the case 10 is indicated with the red arrow in Figure 10 (a). The result (Figure 10 (g-h)) shows that the runlet formation is significantly different from case 8. The concentration distribution (Figure 10 (g)) shows that the width of the runlet is larger in case 10. The increase in runlet width and area is attributed to the aperture variability. In case 10, the right half of the fracture where the lighter fluid is injected has relatively smaller apertures, while the left half of the fracture where the denser fluid is injected has larger apertures. When the lighter fluid flows through the zone with narrower apertures, due to the mass conservation, the flow cross-sectional area of lighter fluid will likely increase. Therefore, in case 10, the runlet width is larger. This is evident from the streamlines (Figure 10 (h)), in which we can observe how the streamlines are dispersed and tend to flow to the area with larger fracture aperture. Furthermore, the streamlines

show that there is only one large stable vortex near the inlet that does not travel upwards. This indicates that the aperture variability can affect the movement of vortices. Results from this section confirms that runlet still appears in rough fractures, but the shape and instability of runlet is sensitive to a given aperture field. In nature, fracture roughness and aperture can vary widely, and thus a more comprehensive study on runlet formation in rough fractures should be an important topic of future study.

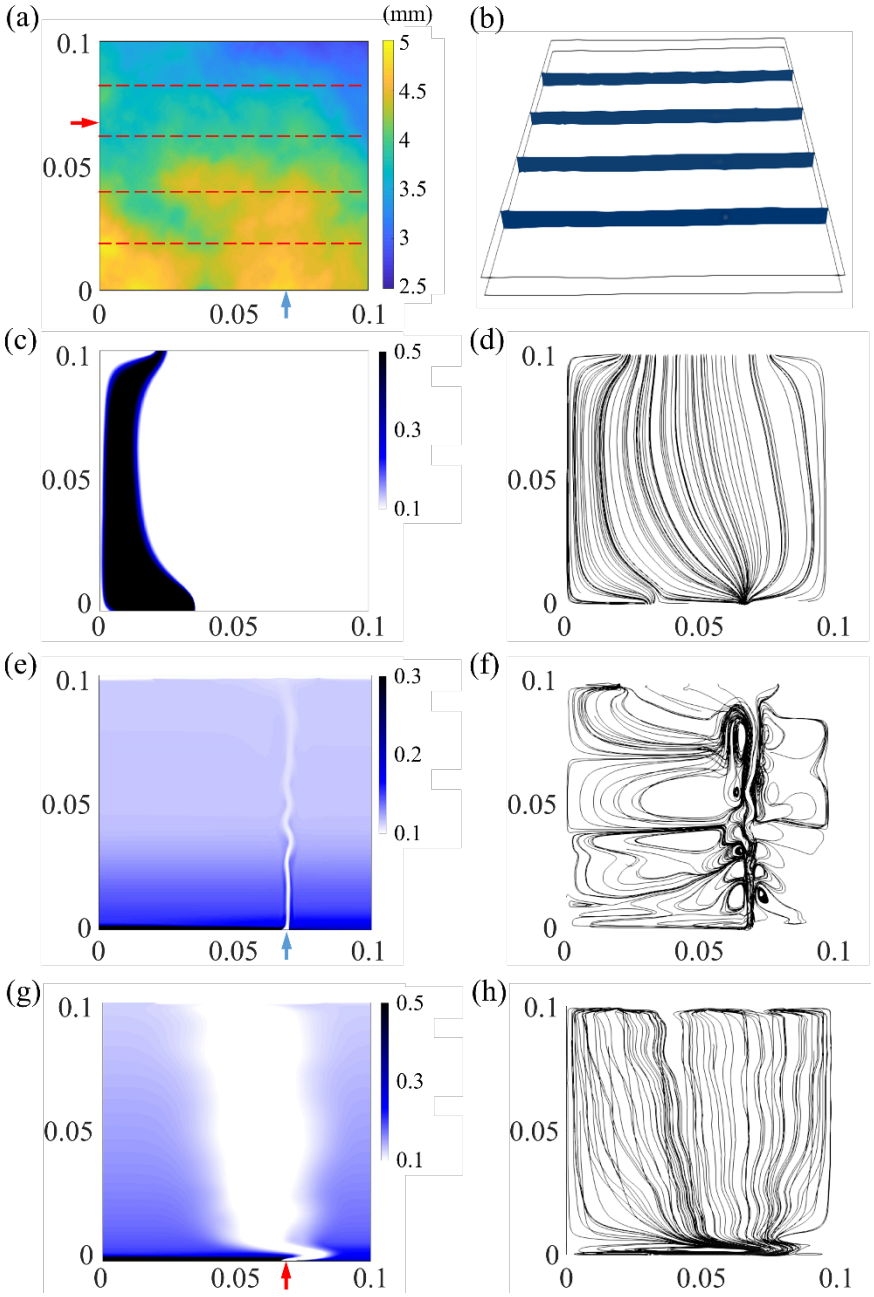

Figure 10. (a) Aperture map formed by two rough fracture surfaces. Dashed lines show cross sectional locations. Blue arrow shows the injection position of lighter fluid in the case 9. Red arrow shows the injection position of lighter fluid in the case 10. For the case 10, we rotate the fracture to place the injection position at the bottom. (b) Cross sections of the rough fracture. (c) Depth averaged concentration distribution of the rough fracture case in which the two fluids have same density at three PVI. (d) Streamlines in the rough fracture case in which the two fluids have same density at three PVI. (e) Depth averaged concentration distribution of the case 9 at three PVI. The unstable runlet is still evident in rough fracture. (f) Streamlines of the case 9 at three PVI. Note the vortices along the runlet. (g) Depth averaged concentration distribution of the case 10 at three PVI. The runlet is wider. (h) Streamlines of the case 10 at three PVI. The streamlines are dispersed due to aperture variability. Cases 9 and 10 are based on the same rough fracture but the injection location is different.

4. Summary and Conclusions

In this study, we investigated variable-density flows in vertical fractures and elucidated the formation and origin of the unstable runlet based on a visual laboratory experiment and direct 3D numerical simulations. Results show that when two fluids with different densities are injected at the bottom of a vertical fracture, the lighter fluid is confined to a narrow runlet which could be unstable. The formation of the runlet requires a sufficient density difference between the fluids, and the mixing of the two fluids is demonstrated to play an important role. If there is no density difference between the two fluids, or if the two fluids are well-mixed, the runlet does not appear.

We identified RTI as the origin of vortices that control the instability of the runlet. The large concentration gradient between the runlet and surrounding fluid, especially at the lower part of the fracture, leads to the emergence of vortices due to the RTI. The estimation of the critical Rayleigh number further confirmed that the instability arises due to the RTI: the estimated Rayleigh number near the inlet is larger than the critical Rayleigh number. Further, flow topology analysis of the velocity field identified vortices, which are shown to be strongly correlated with runlet instability. Vortices emerge due to the RTI near the inlet, and they are

shown to travel along the runlet, controlling the runlet instability. The number of vortices over time showed a very similar trend to the time evolution of the runlet length.

Inertial force is shown to control the effect of vortices on runlet instability. Vortices emerge near the inlet but high local inertial force near the inlet keeps the runlet straight. Due to the injection force, the vortices travel upwards with the flow. In the upper part, where the inertial (injection) force decreases, the vortical flows dominate the shaping of the runlet, making the runlet to be unstable. In the case without inertial force, the instability not only occurs in the upper part of the fracture, but also near the inlet. The vortices that appear near the inlet makes the entire runlet to be unstable due to the lack of inertia. The upward movement of vortices are limited due to the lack of inertia force, but their effects near the inlet affects the entire runlet. The injection rate of the lighter fluid is also shown to control the wavelength of the unstable runlet and size of the vortices. When the injection rate is smaller, which means the inertial force is smaller, the wavelength and size of vortices are smaller. Our results highlight that even in laminar fracture flow conditions, inertia can play a critical role. Finally, we confirmed the formation of unstable runlets in rough fractures, and aperture variability is demonstrated to play an important role in shaping the runlet and its instability.

In this study, various factors affecting the formation and instability of a runlet in a vertical fracture were explored. The results of this study elucidate the underlying mechanisms triggering the instability in variable-density fracture flows and provide insights into the complex interplay between transport, mixing, and runlet instability in a vertical fracture. This study has important implications for the prediction, design, and operation of subsurface processes and applications that involve variable-density fluids in channel flows. For example, the unstable runlet may have strong impact on the extent of seawater intrusion in coastal aquifers. Further, runlet may have even more dramatic effects if dissolution and precipitation reactions are present. The locations of dissolution and precipitation will be a strong function of runlet characteristics, which may control the efficiency of geologic carbon mineralization. The effects of the runlet on dissolution and precipitation reactions in rough fractures is an important topic for future study.

Acknowledgments: PKK and HC acknowledge the support by the National Science Foundation under Grant No. EAR-2046015 and Grant No. CBET-2053413. We thank the Minnesota Supercomputing Institute (MSI) at the University of Minnesota for computational resources and support. LJPN and XZ acknowledge support for the former Center for Nanoscale Controls on Geologic CO_2 (NCGC), an Energy Frontier Research Center funded by the U.S. Department of Energy, Office of Science, Basic Energy Sciences under Award # DE-AC02-05CH11231.

Data Availability Statement

All data and software will be made available by the time of publication through the Data Repository for University of Minnesota (DRUM). https://conservancy.umn.edu/drum The data is being uploaded and we are in the process of obtaining a DOI.

References

Abarbanel, H. D. I., Holm, D. D., Marsden, J. E., & Ratiu, T. (1984). Richardson number criterion for the nonlinear stability of three-dimensional stratified flow. *Physical Review Letters*, *52*(26). https://doi.org/10.1103/PhysRevLett.52.2352

Ahoulou, A. W. A., Tinet, A. J., Oltéan, C., & Golfier, F. (2020). Experimental Insights Into the Interplay Between Buoyancy, Convection, and Dissolution Reaction. *Journal of Geophysical Research: Solid Earth*, *125*(11), e2020JB020854. https://doi.org/10.1029/2020JB020854

Almarcha, C., Trevelyan, P. M. J., Grosfils, P., & de Wit, A. (2010). Chemically driven hydrodynamic instabilities. *Physical Review Letters*, *104*(4). https://doi.org/10.1103/PhysRevLett.104.044501

Al-Bahlani, A. M., & Babadagli, T. (2012). Visual analysis of diffusion process during oil recovery using a Hele-Shaw model with hydrocarbon solvents and thermal methods. *Chemical Engineering Journal*, *181–182*, 557–569. https://doi.org/10.1016/J.CEJ.2011.11.087

Asimov, D. (1993). Notes on the Topology of Vector Fields and Flows. *Proc. of IEEE Visualization*.

Bakker, P.G., Berger, M.S., 1991. Bifurcations in flow patterns: Some applications of the qualitative theory of differential equations in fluid dynamics, Nonlinear Topics in the Mathematical Sciences. Springer Netherlands. https://doi.org/10.1007/978-94-011-3512-2

Bouquain, J., Meheust, Y., & Davy, P. (2011). Horizontal pre-asymptotic solute transport in a plane fracture with significant density contrasts. *Journal of Contaminant Hydrology*, *120–121*(C), 184–197. https://doi.org/10.1016/j.jconhyd.2010.08.002

Bresciani, E., Kang, P. K., & Lee, S. (2019). Theoretical Analysis of Groundwater Flow Patterns Near Stagnation Points. *Water Resources Research*. https://doi.org/10.1029/2018WR023508

Bujack, R., Tsai, K., Morley, S. K., & Bresciani, E. (2021). Open source vector field topology. *SoftwareX*, *15*. https://doi.org/10.1016/j.softx.2021.100787

Cengel, Y., Turner, R., & Smith, R. (2001). Fundamentals of Thermal-Fluid Sciences . *Applied Mechanics Reviews*, *54*(6). https://doi.org/10.1115/1.1421126

Chaudhuri, A., Rajaram, H., Viswanathan, H., Zyvoloski, G., & Stauffer, P. (2009). Buoyant convection resulting from dissolution and permeability growth in vertical limestone fractures. *Geophysical Research Letters*, *36*(3). https://doi.org/10.1029/2008GL036533

Chen, J. D. (1989). Growth of radial viscous fingers in a Hele-Shaw cell. *Journal of Fluid Mechanics*, *201*, 223-242. https://doi.org/10.1017/S0022112089000911

Chiogna, G., Cirpka, O.A., Rolle, M., & Bellin, A. (2015). Helical flow in three-dimensional nonstationary anisotropic heterogeneous porous media. *Water Resources Research*. 51, 261–280. https://doi.org/10.1002/2014WR015330

Cirpka, O. A., Chiogna, G., Rolle, M., & Bellin, A. (2015). Transverse mixing in three-dimensional nonstationary anisotropic heterogeneous porous media. *Water Resources Research*, *51*(1). https://doi.org/10.1002/2014WR015331

Cohen, C., Berhanu, M., Derr, J., & Courrech Du Pont, S. (2020). Buoyancy-driven dissolution of inclined blocks: Erosion rate and pattern formation. *Physical Review Fluids*, *5*(5). https://doi.org/10.1103/PhysRevFluids.5.053802

Contreras, P.S., Speetjens, M.F.M., & Clercx, H.J.H. (2017). Lagrangian transport in a class of three-dimensional buoyancy-driven flows. *Journal of Fluid Mechanics*. 832, 5-40. https://doi.org/10.1017/jfm.2017.680

de Barros, F. P. J., Dentz, M., Koch, J., & Nowak, W. (2012). Flow topology and scalar mixing in spatially heterogeneous flow fields. *Geophysical Research Letters*, *39*(8). https://doi.org/10.1029/2012GL051302

Délery, J. (2013). Three-dimensional separated flows topology: singular points, beam splitters and vortex structures. John Wiley & Sons, Somerset, NJ, USA.

Dentz, M., le Borgne, T., Englert, A., & Bijeljic, B. (2011). Mixing, spreading and reaction in heterogeneous media: A brief review. In *Journal of Contaminant Hydrology* (Vols. 120-121, Issue C). https://doi.org/10.1016/j.jconhyd.2010.05.002

Dietrich, P., Helmig, R., Sauter, M., Teutsch, G., Hötzl, H., & Köngeter, J. (2005). Flow and transport in fractured porous media. *Flow and Transport in Fractured Porous Media*, 1-447. https://doi.org/10.1007/B138453/COVER

Fernandez, J., Kurowski, P., Petitjeans, P., & Meiburg, E. (2002). Density-driven unstable flows of miscible fluids in a Hele-Shaw cell. *Journal of Fluid Mechanics*, *451*. https://doi.org/10.1017/s0022112001006504

Funada, T., & Joseph, D. D. (2001). Viscous potential flow analysis of Kelvin-Helmholtz instability in a channel. *Journal of Fluid Mechanics*, *445*, 261-283. https://doi.org/10.1017/s0022112001005572

Galperin, B., Sukoriansky, S., & Anderson, P. S. (2007). On the critical Richardson number in stably stratified turbulence. *Atmospheric Science Letters*, *8*(3), 65-69. https://doi.org/10.1002/asl.153

Gartling, D. K., & Hickox, C. E. (1985). A numerical study of the applicability of the Boussinesq approximation for a fluid-saturated porous medium. *International Journal for Numerical Methods in Fluids*, *5*(11). https://doi.org/10.1002/fld.1650051105

Globus, A., Levit, C., & Lasinski, T. (1991). A tool for visualizing the topology of three-dimensional vector fields. *Proceedings of the 2nd Conference on Visualization 1991, VIS 1991*. https://doi.org/10.1109/visual.1991.175773

Graf, T., & Therrien, R. (2005). Variable-density groundwater flow and solute transport in porous media containing nonuniform discrete fractures. *Advances in Water Resources*, *28*(12), 1351-1367. https://doi.org/10.1016/j.advwatres.2005.04.011

Graf, T., & Therrien, R. (2007). Variable-density groundwater flow and solute transport in irregular 2D fracture networks. *Advances in Water Resources*, *30*(3), 455-468. https://doi.org/10.1016/j.advwatres.2006.05.003

Gray, D. D., & Giorgini, A. (1976). The validity of the boussinesq approximation for liquids and gases. *International Journal of Heat and Mass Transfer*, *19*(5). https://doi.org/10.1016/0017-9310(76)90168-X

Günther, A., & Jensen, K. F. (2006). Multiphase microfluidics: from flow characteristics to chemical and materials synthesis. *Lab on a Chip*, *6*(12), 1487-1503. https://doi.org/10.1039/B609851G

Hage, E., & Tilgner, A. (2010). High Rayleigh number convection with double diffusive fingers. *Physics of Fluids*, *22*(7), 1-7. https://doi.org/10.1063/1.3464158

Hamimid, S., Guellal, M., & Bouafia, M. (2021). Limit of the buoyancy ratio in Boussinesq approximation for double-diffusive convection in binary mixture. *Physics of Fluids*, *33*(3). https://doi.org/10.1063/5.0037320

Helman, J., & Hesselink, L. (1989). Representation and Display of Vector Field Topology in Fluid Flow Data Sets. *Computer*, *22*(8). https://doi.org/10.1109/2.35197

He, X., Zhang, R., Chen, S., & Doolen, G. D. (1999). On the three-dimensional Rayleigh-Taylor instability. *Physics of Fluids*, *11*(5), 1143-1152. https://doi.org/10.1063/1.869984

Hidalgo, J.J., & Dentz, M. (2018). Mixing across fluid interfaces compressed by convective flow in porous media. *Journal of Fluid Mechanics*. *838*, 105-128. https://doi.org/10.1017/jfm.2017.888

Howard, L. N. (1961). Note on a paper of John W. Miles. *Journal of Fluid Mechanics*, *10*(4). https://doi.org/10.1017/S0022112061000317

Huang, J. mac, Tong, J., Shelley, M., & Ristroph, L. (2020). Ultra-sharp pinnacles sculpted by natural convective dissolution. *PNAS*, *117*. https://doi.org/10.1073/pnas.2001524117

Kang, P. K., Brown, S., & Juanes, R. (2016). Emergence of anomalous transport in stressed rough fractures. *Earth and Planetary Science Letters*, *454*. https://doi.org/10.1016/j.epsl.2016.08.033

751 Kneafsey, T. J., & Pruess, K. (2010). Laboratory flow experiments for visualizing carbon
752 dioxide-induced, density-driven brine convection. *Transport in Porous Media*, *82*(1), 123–
753 139. https://doi.org/10.1007/s11242-009-9482-2
754 Kull, H. J. (1991). Theory of the Rayleigh-Taylor instability. In *Physics Reports* (Vol. 206, Issue
755 5). https://doi.org/10.1016/0370-1573(91)90153-D
756 le Borgne, T., Dentz, M., & Villermaux, E. (2013). Stretching, coalescence, and mixing in
757 porous media. *Physical Review Letters*, *110*(20).
758 https://doi.org/10.1103/PhysRevLett.110.204501
759 le Quere, P. (1990). *A Note on Multiple and Unsteady Solutions in Two-Dimensional Convection*
760 *in a Tall Cavity*. http://asmedigitalcollection.asme.org/heattransfer/article-
761 pdf/112/4/965/5651934/965_1.pdf
762 Lee, S. H., & Kang, P. K. (2020). Three-Dimensional Vortex-Induced Reaction Hot Spots at
763 Flow Intersections. *Physical Review Letters*, *124*.
764 https://doi.org/10.1103/PhysRevLett.124.144501
765 Lester, D.R., Metcalfe, G., Trefry, M.G., Ord, A., Hobbs, B., & Rudman, M. (2009). Lagrangian
766 topology of a periodically reoriented potential flow: symmetry, optimization, and mixing.
767 *Physical Review E*. *80*(3), 036208-1 - 036208-10.
768 https://doi.org/10.1103/PhysRevE.80.036208
769 Morijiri, T., Sunahiro, S., Senaha, M., Yamada, M., & Seki, M. (2011). Sedimentation pinched-
770 flow fractionation for size- and density-based particle sorting in microchannels.
771 *Microfluidics and Nanofluidics*, *11*(1), 105–110. https://doi.org/10.1007/S10404-011-0785-
772 6/TABLES/2
773 Oltéan, C., Golfier, F., & Buès, M. A. (2013). Numerical and experimental investigation of
774 buoyancy-driven dissolution in vertical fracture. *Journal of Geophysical Research: Solid*
775 *Earth*, *118*(5), 2038-2048. https://doi.org/10.1002/jgrb.50188
776 Ott, H., & Oedai, S. (2015). Wormhole formation and compact dissolution in single- and two-
777 phase CO2-brine injections. *Geophysical Research Letters*, *42*(7), 2270-2276.
778 https://doi.org/10.1002/2015GL063582

Park, H. Y., Jang, K., Ju, J. W., & Yeo, I. W. (2012). Hydrogeological characterization of seawater intrusion in tidally-forced coastal fractured bedrock aquifer. *Journal of Hydrology*, *446-447*, 77-89. https://doi.org/10.1016/j.jhydrol.2012.04.033

Perko, L. (2001). Differential equations and dynamical systems, 3rd ed. Springer New York, New York, NY.

Perry, A. E., & Fairlie, B. D. (1975). Critical points in flow patterns. *Advances in Geophysics*, *18*(PB). https://doi.org/10.1016/S0065-2687(08)60588-9

Perry, A.E., & Chong, M.S. (1994). Topology of flow patterns in vortex motions and turbulence. *Applied Scientific Research*. *53*, 357-374. https://doi.org/10.1007/bf00849110

Portarapillo, M., & di Benedetto, A. (2021). Risk Assessment of the Large-Scale Hydrogen Storage in Salt Caverns. *Energies 2021, Vol. 14, Page 2856*, *14*(10), 2856. https://doi.org/10.3390/EN14102856

Romanò, F., Albensoeder, S., & Kuhlmann, H.C. (2017). Topology of three-dimensional steady cellular flow in a two-sided anti-parallel lid-driven cavity. *Journal of Fluid Mechanics*. *826*, 302-334. https://doi.org/10.1017/jfm.2017.422

Ronen, D., Yechieli, Y., & Kribus, A. (1995). Buoyancy-induced flow of a tracer in vertical conduits. *Water Resources Research*, *31*(5), 1167-1173. https://doi.org/10.1029/95

Saffman, P. G., & Taylor, G. I. (1958). The penetration of a fluid into a porous medium or Hele-Shaw cell containing a more viscous liquid. *Proceedings of the Royal Society of London. Series A. Mathematical and Physical Sciences*, *245*(1242), 312-329. https://doi.org/10.1098/rspa.1958.0085

Sawayama, K., Ishibashi, T., Jiang, F., Tsuji, T., Nishizawa, O., & Fujimitsu, Y. (2021). Scale-independent relationship between permeability and resistivity in mated fractures with natural rough surfaces. *Geothermics*, *94*. https://doi.org/10.1016/j.geothermics.2021.102065

Sexton, A., Punch, J., Stafford, J., & Jeffers, N. (2018). The thermal and hydrodynamic behaviour of confined, normally impinging laminar slot jets. *International Journal of Heat and Mass Transfer*, *123*, 40–53. https://doi.org/10.1016/j.ijheatmasstransfer.2018.02.083

Sharp, D. H. (1984). An overview of Rayleigh-Taylor instability. *Physica D: Nonlinear Phenomena*, *12*(1–3). https://doi.org/10.1016/0167-2789(84)90510-4

Shikaze, S. G., Sudicky, E. A., & Schwartz, F. W. (1998). Density-dependent solute transport in discretely-fractured geologic media: Is prediction possible? *Journal of Contaminant Hydrology*, *34*(3). https://doi.org/10.1016/S0169-7722(98)00080-1

Simmons, C. T. (2005). Variable density groundwater flow: From current challenges to future possibilities. *Hydrogeology Journal*, *13*(1), 116–119. https://doi.org/10.1007/s10040-004-0408-3

Sivasamy, A., Selladurai, V., & Rajesh Kanna, P. (2007). Numerical simulation of two-dimensional laminar slot-jet impingement flows confined by a parallel wall. *International Journal for Numerical Methods in Fluids*, *55*(10). https://doi.org/10.1002/fld.1492

Ślezak, A., Dworecki, K., Jasik-Ślezak, J., & Wasik, J. (2004). Method to determine the critical concentration Rayleigh number in isothermal passive membrane transport processes. *Desalination*, *168*(1–3). https://doi.org/10.1016/j.desal.2004.07.027

Smyth, W. D., & Moum, J. N. (2012). Ocean mixing by Kelvin-Helmholtz instability. *Oceanography*, *25*(2). https://doi.org/10.5670/oceanog.2012.49

Snippe, J., Gdanski, R., & Ott, H. (2017). Multiphase Modelling of Wormhole Formation in Carbonates by the Injection of CO2. *Energy Procedia*, *114*, 2972–2984. https://doi.org/10.1016/j.egypro.2017.03.1426

Solano, T., Ordonez, J. C., & Shoele, K. (2022). Natural convection in vertical enclosures with conjugate boundary conditions. *Journal of Fluid Mechanics*, *946*, A17. https://doi.org/10.1017/jfm.2022.568

Stein, R.F., Nordlund, A., Stein, R.F., & Nordlund, A. (1989). Topology of convection beneath the Solar Surface. *The Astrophysical Journal*, *342*, L95-L98. https://doi.org/10.1086/185493

Tenchine, S., & Gouze, P. (2005). Density contrast effects on tracer dispersion in variable aperture fractures. *Advances in Water Resources*, *28*(3), 273–289. https://doi.org/10.1016/j.advwatres.2004.10.009

Theisel, H., Rössl, C., & Weinkauf, T. (2008). Topological representations of vector fields. In *Mathematics and Visualization* (Vol. 0, Issue 9783540332640). https://doi.org/10.1007/978-3-540-33265-7_7

Theisel, H., Weinkauf, T., Hege, H.C., & Seidel, H.P. (2005). Topological methods for 2D time-dependent vector fields based on stream lines and path lines. *IEEE Transactions on*

838 *Visualization and Computer Graphics*, *11*(4), 383-394.
839 https://doi.org/10.1109/TVCG.2005.68

840 Tongwa, P., Nygaard, R., Blue, A., & Bai, B. (2013). Evaluation of potential fracture-sealing
841 materials for remediating CO2 leakage pathways during CO2 sequestration. *International*
842 *Journal of Greenhouse Gas Control*, *18*, 128–138.
843 https://doi.org/10.1016/j.ijggc.2013.06.017

844 Trevelyan, P. M. J., Almarcha, C., & de Wit, A. (2011). Buoyancy-driven instabilities of
845 miscible two-layer stratifications in porous media and Hele-Shaw cells. *Journal of Fluid*
846 *Mechanics*, *670*, 38–65. https://doi.org/10.1017/S0022112010005008

847 Tryggvason, G. (1988). Numerical simulations of the Rayleigh-Taylor instability. *Journal of*
848 *Computational Physics*, *75*(2). https://doi.org/10.1016/0021-9991(88)90112-X

849 Tsang, C. F., & Neretnieks, I. (1998). Flow channeling in heterogeneous fractured rocks.
850 *Reviews of Geophysics*, *36*(2), 275–298. https://doi.org/10.1029/97RG03319

851 Weller, H. G., Tabor, G., Jasak, H., & Fureby, C. (1998). A tensorial approach to computational
852 continuum mechanics using object-oriented techniques, *Computers in physics*, *12*(6), 620-
853 631. http://dx.doi.org/10.1063/1.168744

854 Wood, B. D., He, X., & Apte, S. V. (2020). Modeling turbulent flows in porous media. *Annual*
855 *Review of Fluid Mechanics*, *52*, 171-203. https://doi.org/10.1146/annurev-fluid-010719-
856 060317

857 Wooding, R. A., Tyler, S. W., & White, I. (1997). Convection in groundwater below an
858 evaporating salt lake: 1. Onset of instability. *Water Resources Research*, *33*(6).
859 https://doi.org/10.1029/96WR03533

860 Xu, X., Cao, H., Yoon, S., Kang, P. K., Jun. Y., Kneafsey, T., Cole, D., & Pyrak-Nolte., L. J.
861 (2022). Gravity-driven controls on fluid and precipitate distributions in fractures.
862 [Submitted for publication]

863 Yamato, P., Tartèse, R., Duretz, T., & May, D. A. (2012). Numerical modelling of magma
864 transport in dykes. *Tectonophysics*, *526–529*, 97–109.
865 https://doi.org/10.1016/j.tecto.2011.05.015

Yoon, S., Dentz, M., & Kang, P. K. (2021). Optimal fluid stretching for mixing-limited reactions in rough channel flows. *Journal of Fluid Mechanics*, *916*, A45. https://doi.org/10.1017/jfm.2021.208

Yoon, S., & Kang, P. K. (2021). Roughness, inertia, and diffusion effects on anomalous transport in rough channel flows. *Physical Review Fluids*, *6*(1), 014502. https://doi.org/10.1103/PhysRevFluids.6.014502

Zalts, A., el Hasi, C., Rubio, D., Ureña, A., & D'Onofrio, A. (2008). Pattern formation driven by an acid-base neutralization reaction in aqueous media in a gravitational field. *Physical Review E - Statistical, Nonlinear, and Soft Matter Physics*, *77*(1). https://doi.org/10.1103/PhysRevE.77.015304